ADVANCED FUNCTIONAL MATERIALS
www.afm-journal.de

Improved Charge Recombination Efficiency in Organic Light-Emitting Transistors via Luminescent Radicals

Francesco Reginato, Eugenio Lunedei, Sara Mattiello, Giulia Baroni, Margherita Bolognesi, Francesco Porcelli, Giuseppe Mattioli, Yohei Hattori, Mario Prosa, Luca Beverina, and Stefano Toffanin**

Luminescent radicals are attracting attention as emitters in electroluminescent devices thanks to the exploitation of doublet excitons. Recent studies reveal that exciton formation in radical organic light-emitting diodes (OLEDs) primarily occurs through a charge trapping mechanism. Although typically detrimental for OLEDs, this might be a key process to elucidate light emission in organic light-emitting transistors (OLETs). Here, a unipolar n-type architecture suitable for the implementation of radical emitters is introduced, designed based on computational calculations. The operation of the as-realized devices incorporating the newly synthesized [2,6-dichloro-4-(2,6-dimethoxyphenyl)phenyl](3,5-dichloro-4-pyridyl)(2,4,6-trichlorophenyl)methyl radical is investigated via transient electroluminescence measurements to demonstrate the occurrence of long-living emission ascribed to the charge trapping mechanisms. Moreover, a comprehensive understanding of the processes governing radical-OLET is obtained by recording complete 2D maps of both optical and electrical response of the device as a function of applied voltages. Notably, the trapping of electrons by radical moieties is demonstrated to generate a negative charge density in the emissive layer that facilitates holes to be injected: increasing the balance of opposite charge carriers, a tenfold enhancement of the external quantum efficiency (EQE) at the proper source-drain and source-gate voltage conditions is reported to reach a maximum EQE value of 0.2%.

1. Introduction

Organic light-emitting transistors (OLETs) represent an emerging class of optoelectronic devices in which light generation and electrical switching characteristics are simultaneously provided by a planar architecture comprising multiple functional layers.[1–4] Similar to organic field-effect transistors (OFETs), OLETs are three terminal devices employing π-conjugated organic semiconductors (OSCs) and organic/inorganic insulators as the active channel material and dielectric layer, respectively. In particular, OLETs attracted considerable interest because of their planar device architecture making them innovative light sources in integrated systems,[5,6] with the peculiar advantages to simplify the overall electrical circuitry and to exploit the cost-effective fabrication processes and inherent multifunctionality of OSCs.[7–10] Considering an ambipolar single-layer OLET, the radiative recombination of opposite charges takes place within the transistor channel with the emission region being tens micrometers wide.[11–13] The great potential of ambipolar OLETs is that the presence of three terminals permits to tune the transistor transconductance, thus the lengths of the electron and hole channels and eventually the location of the emission zone within the device channel. Nevertheless, the development of efficient ambipolar single-layer OLETs is hampered by the lack of OSCs with both balanced ambipolar charge transport and high electroluminescence yield.[11,14] In this context, a breakthrough was achieved by

F. Reginato, E. Lunedei, G. Baroni, M. Bolognesi, M. Prosa, S. Toffanin
Institute of Nanostructured Materials (ISMN) – National Research Council (CNR)
Via P. Gobetti 101, Bologna 40129, Italy
E-mail: mario.prosa@cnr.it; stefano.toffanin@cnr.it

The ORCID identification number(s) for the author(s) of this article can be found under https://doi.org/10.1002/adfm.202411845

DOI: 10.1002/adfm.202411845

S. Mattiello, L. Beverina
Department of Materials Science
University of Milano-Bicocca
Via R. Cozzi, 55, Milano 20126, Italy

F. Porcelli, G. Mattioli
Istituto di Struttura della Materia – National Research Council (ISM-CNR)
Area della Ricerca di Roma 1, Via Salaria km 29.300, Monterotondo 00015, Italy

Y. Hattori
Division of Materials Science
Nara Institute of Science and Technology
8916-5 Takayama-cho, Ikoma, Nara 630-0192, Japan

introducing multilayered OLET architectures,[15–17] in which charge transport and light emission are provided by different layers so that both electrical and optical characteristics can be finely optimized to boost the OLET performance. Indeed, one of the most used architectures consists of two active layers (bilayer architecture) where a single and efficient charge transporting semiconductor layer provides a high density of charges into the emissive layer (EML), even though the distinguishing feature of gate-bias controlled spatial tuning of the emission stripe cannot be any longer be observed since only one type of charge carrier can flow in the transistor channel. The unipolar nature of the device requires minority charge carriers to be injected from the drain electrode into the EML to promote the radiative recombination with major carriers.[18] To tackle this issue, different approaches have been introduced over the years such as implementing new device architectures or including additional layers in traditional structures to favor the selective injection of charge carriers.[19] Nevertheless, the typically poor balance between lateral flow of major carriers and vertical injection of opposite charges results in low efficiency that remains a major limitation of the technology.[3,20–23] In addition to that, intrinsic losses are also affecting the device external quantum efficiency (EQE) as a result of the suboptimal efficiency of the EML to convert free charges into photons, as occurring in organic light emitting diodes (OLEDs), due to limitations of spin statistics in organic emitters.

Recently, luminescent radicals have been attracting considerable interest as emitting materials in optoelectronics due to their intrinsic ability to overcome the spin statistic limitation of the most common singlet organic emitters, thus representing a cost-effective alternative to phosphorescent organometallic ones.[24] Organic radical emitters have unpaired electrons that allow exploiting the electroluminescence from doublet excitons rather than undergoing typical limitations due to singlet and triplet exciton conversion in closed-shell molecules. Being both the ground state and the excited state spin doublet, these systems could in principle reach the internal quantum efficiency (IQE) of 100%.[25] Since the development of the first radical-based OLED in 2015 by Peng et al.,[26] advances have been achieved both in the synthesis of highly luminescent radical emitters[27–34] and in their integration into efficient OLEDs[24,26,35–41] obtaining a state-of-the-art radical OLED with near-unity internal quantum efficiency (IQE) and the EQE as high as 27%.[24] Recently it has been demonstrated that the recombination of charge carriers in radical OLEDs largely occurs through a charge trapping mechanism, in which under electrical excitation radical emitters tend to trap electrons and then holes interact with trapped charges to form excitons.[42,43] While charge trapping is typically considered an undesired process in OLEDs as it is detrimental for the charge transport characteristics,[44] it might be a key process to enable light emission in OLETs. In fact, the electroluminescence mechanism that governs exciton formation in unipolar OLETs has been described as a two-step process where the intense electric field at the proximity of the drain electrode is responsible for the injection of the minority charges in the EML which meet trapped major carriers at the emissive sites.[12,45] However, this mechanism has never been fully demonstrated. In this framework, the advantage of using radical emitters as charge recombination sites in the EML in OLETs is twofold: i) to elucidate the mechanism governing the radiative recombination to fully exploit it, ii) to optimize light-formation processes by using doublet excitons. The organic radical emitters typically used in optoelectronic devices present low-lying highest occupied molecular orbital (HOMO) energy levels (generally lower than −6 eV):[25,46] this in turn may represent a stringent impediment to the use of these materials in OLETs since the restricted portfolio of hole transporting OSCs with HOMO levels that can suitably match with those of the radical emitters. Indeed, the majority of unipolar OLETs use p-type OSCs as the active semiconducting layer in the channel due to the multiple choices in the selection of compounds with good energy alignment with the overlying host–guest EML.[20–22,47] The energy mismatch in the case of radical emitters could be addressed by using n-type OSCs in the device structure so that the low-lying singly unoccupied molecular orbital (SUMO) level of the radical may match the lowest unoccupied molecular orbital (LUMO) energy level of the OSC. However, n-type OSCs are generally less available than the p-type counterparts. Differently from n-type inorganic semiconductors that are widely used in the so-called hybrid light-emitting transistors, only few examples of n-type OSCs in OLETs have been reported.[48–53]

In this study, we engineered and realized a unipolar n-type OLET structure suitable for the implementation of organic radical emitters. Moreover, the device was implemented as a platform for investigating charge trapping in the emissive layer as the preferential mechanism for exciton formation in OLET. To the best of our knowledge, organic radicals have never been reported in light-emitting transistors to date. Among radical emitters, we chose to use PyBTM-like radicals that are a class of persistent open-shell derivatives with large Stokes shift that limits self-absorption phenomena and that were successfully integrated not only in OLEDs,[37] but also in other optoelectronic devices like solar concentrators.[54] With respect to other triarylmethane derivatives already employed in light emitting devices,[24] the presence of the pyridine ring in the PyBTM family ensures a dramatically improved photostability.[55] Thus, [2,6-dichloro-4-(2,6-dimethoxyphenyl)phenyl](3,5-dichloro-4-pyridyl) (2,4,6-trichlorophenyl)methyl radical (PyBTM-(Me2Res)) was synthesized according to a modification of a previously reported green chemistry compliant methodology[54] and employed as radical emitter and used as guest in 2,2′,2″-(1,3,5-benzinetriyl)-tris(1-phenyl-1-*H*-benzimidazole) (TPBi) n-type matrix to form a host–guest EML. Then, an appropriate OSC was selected in order to guarantee good field-effect charge transport and effective charge injection into the EML: *N*,*N*′-ditridecylperylene-3,4,9,10-tetracarboxylic diimide (P13) fulfills these requirements to be used as the active channel n-type OSC in the OLET.[10] Finally, 4,4′-bis(9-carbazolyl)-1,1′-biphenyl (CBP) was used as hole injection layer (HIL) to improve the device optoelectronic performance. The optimization of the concentration of the radical emitter in the host matrix with respect to the emitted optical power highlighted the possible role of electron trapping in exciton formation. The investigation of the temporal evolution of the EL signal of the best performing device provided solid evidence to the photophysical processes at the basis of the working mechanisms of the OLET. Furthermore, we carried out an in-depth analysis of the functional behavior of the current – voltage characteristics of the devices to obtain 2D map of the external quantum efficiency (EQE) that allowed to identify

non-trivial bias working conditions at which the EQE is ten-fold increased. By the direct comparison with identical OLET devices comprising more traditional emissive guests in the EML that are typical singlet acceptors in energy-transfer process, we demonstrated that the increase of the EQE in radical-OLETs at the proper source-drain and source-gate voltage conditions was due to a threefold improvement of the balance of opposite charge carriers when recombing and leading to electroluminescence.

Collectively, these findings pave the way for implementing luminescent persistent radicals in OLETs by enhancing control over charge accumulation and recombination in 3-terminal devices.

2. Results and Discussion

To develop radical-OLETs (r-OLETs), it is mandatory to engineer a device architecture that is suitable in terms of energy alignment to include organic radical emitters. Quantum mechanical calculations were carried out to investigate the energies of the frontier orbitals of PyBTM-(Me2Res) (**Figure 1a**). Closed-shell HOMO and HOMO-1 orbitals are practically degenerate in both the α and β spin channels (Table S1, Supporting Information) and they show strong localization on the di-methoxy benzene ring. Like in the case of PyBTM[27,54] and its previously investigated benzene derivatives,[30] closed-shell LUMO and LUMO+1 orbitals are primarily localized on the dichloropyridine moiety, which acts as the electron-accepting component, and on the two benzene rings, respectively. Present DFT simulations indicate for PyBTM-(Me2Res) a HOMO-LUMO gap of 4.50 eV, with an electron-donating effect of the single 2,5-dimethoxyphenyl substituent raising the HOMO orbitals of the parent PyBTM radical by 0.9 eV. Such an effect lies between those induced in the phenyl (PyPBTM, 4.86 eV) and in the 9-phenantril (PyPhBTM, 4.32 eV) disubstituted molecules,[54] as detailed in Table S1 (Supporting Information).

The unpaired electron is accommodated in the α-SOMO at −5.68 eV, which is situated within the HOMO–LUMO gap. This orbital is predominantly centered on the radical carbon atom and is complemented by a corresponding unoccupied β-SUMO, which has an energy of −3.50 eV. This energy distribution of molecular orbitals is compatible with oxidation (E[0/+]) and reduction (E[0/-]) potentials calculated in CH_2Cl_2 solution: i.e., −5.84 and −4.05 eV, respectively (Figure 1c).

Typically, the orbitals of radical emitters that are involved in the lowest-energy exciton formation process are the SUMO and HOMO.[43] The latter is calculated as the free energy difference between the $[PyBTM\text{-}(Me2Res)]^-$ anion and the $[PyBTM\text{-}(Me2Res)]^*$ first excited state, placed at −6.23 eV. Thus electron-transporting TPBi (Figure 1b), having a tabulated HOMO level of −6.35 eV, was identified as a wide-bandgap matrix suitable for hosting PyBTM-(Me2Res) (Figure 1c).[56] Considering the E[0/-] reduction potential of −4.05 eV of PyBTM-(Me2Res), an efficient exciton generation process is expected to occur in the designed host:guest emissive system as a result of the SUMO-HOMO energy gap of the radical emitter falling within the HOMO-LUMO energy gap of the TPBi matrix.

Prior to develop r-OLETs, the electrical operation of guest-free devices was verified by fabricating OFETs onto transparent glass/ITO substrates in a bottom-gate/top-contacts configuration with poly(methyl methacrylate) (PMMA) acting as dielectric layer, P13 as n-type semiconductor, TPBi as charge recombination layer, and using Au coplanar source and drain electrodes. Gold was chosen due to its high work function (5.37 eV)[57] to facilitate the injection of holes into TPBi HOMO in view of the OLET realization, being holes the minority charge carriers. The n-type output and transfer characteristic curves of P13-based OFETs are reported in Figure S1 (Supporting Information). Good device operation was obtained, as evidenced by the extrapolated electron mobility (μ_e) as high as 0.25 $cm^2\ V^{-1}\ s^{-1}$ which is in close agreement with that of state-of-the-art single-layer OFETs based on P13.[58–60] To note, the presence of TPBi induced a remarkable reduction of the threshold gate voltage (V_{th}) of the device, that is lowered from 14.0 V to 3.4 V (Table S2, Supporting Information) thus suggesting a beneficial effect on electron injection barrier of P13 OFETs.

Considering the realization of a host–guest EML, the energetics of TPBi matrix could allow the formation of excitons into PyBTM-(Me2Res) by Förster energy transfer, in virtue of the spectral overlap between TPBi host emission and PyBTM-(Me2Res) strong guest SOMO→[LUMO, LUMO+1] absorption peak in the UV region (Figure S2, Supporting Information), as it is typically exploited in OLEDs,[61] but it cannot be excluded that electrons might be directly transferred into the PyBTM-(Me2Res) from TPBi in virtue of the suitable alignment of the SUMO (−4.05 eV) and LUMO (−2.19 eV) levels, respectively. In this context, we investigated blends of TPBi:PyBTM-(Me2Res) at different doping concentrations such as 5%, 15%, and 20% in order to evaluate the efficiency of the possible energy transfer process and to measure the related photoluminescence quantum yields (PLQY) of the emissive species with the purpose of identifying the optimal concentration enabling effective electroluminescence in OLETs. By optically exciting the host matrix at 325 nm, a clear emission from PyBTM-(Me2Res) was observed at ≈655 nm demonstrating a good energy transfer process between the host and the guest compounds (Figure S3, Supporting Information). A negligible red shift of the emission, that is <10 nm, was recorded as the doping concentration increased to 20%, while a residual contribution ascribed to the emission of TPBi is visible in all emission spectra at ≈385 nm (even though decreasing with increasing the doping concentration, as expected). The calculated PLQY was 0.18, 0.15, and 0.13, respectively for the doping concentration of 5%, 15%, and 20% thus a decrease in efficiency in radiative deactivation of the excitons formed by energy transfer is observed as the concentration of the radical guest increases. Based on purely photophysical considerations, 5% PyBTM-(Me2Res) in TPBi should be the most promising blend to be used as EML in OLET considering that its corresponding PLQY closely matches that measured on the pure radical emitter dispersed in a transparent PMMA matrix (1% w/w), which amounted to 0.22.

All the tested concentrations of PyBTM-(Me2Res) were included in the EML to fabricate complete OLET devices. As shown in **Table 1**, all devices showed good electrical characteristics and light emission was observed from each r-OLET, regardless of the guest concentration (Figure S4, Supporting Information). The amount of radical emitters in the EML played a significant influence on the device features. In particular, the higher the PyBTM-(Me2Res) concentration the lower the collected maximum I_{DS}. The electron mobility decreased from 0.2 to 0.06 cm^2

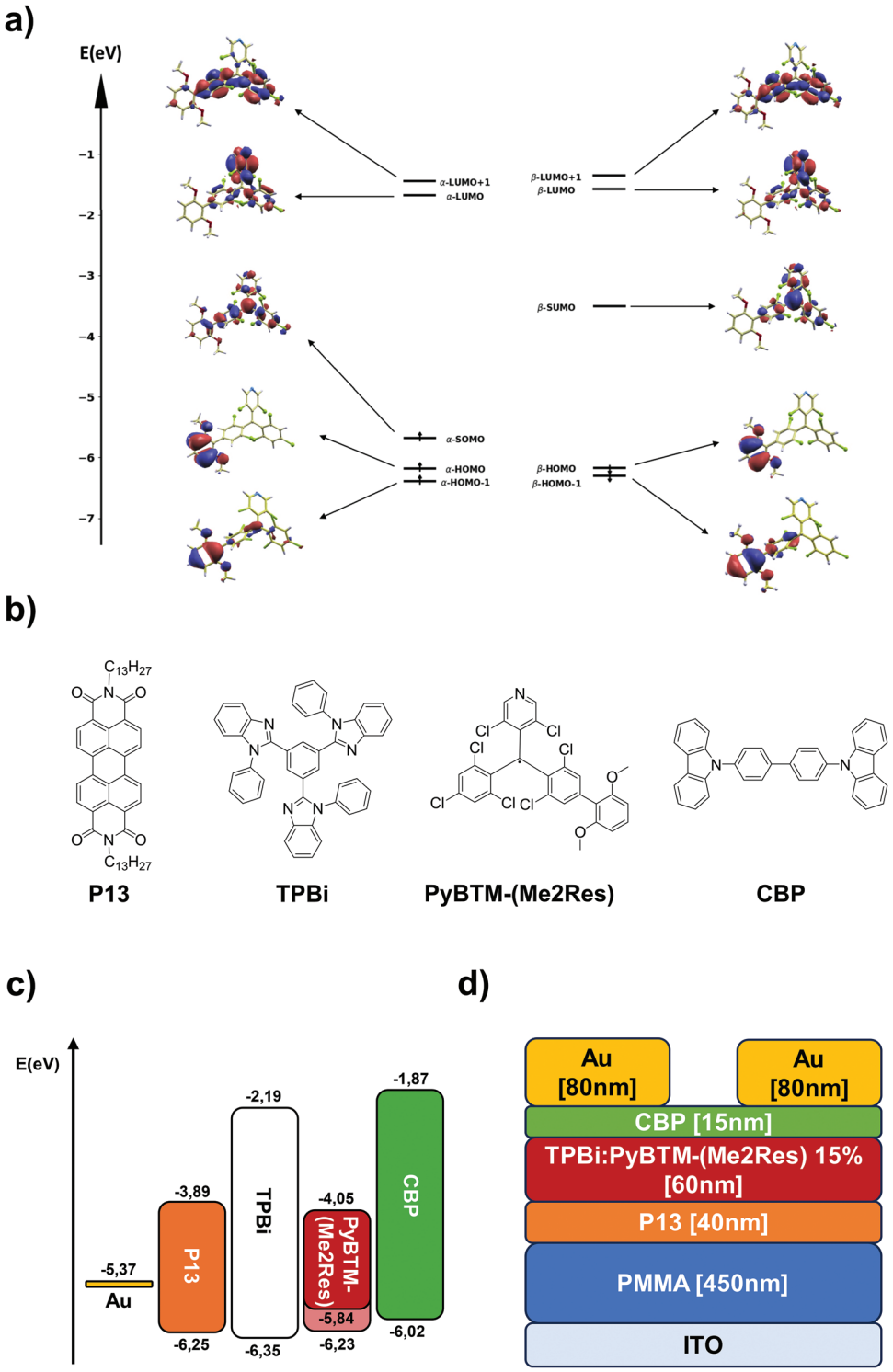

Figure 1. a) Unrestricted Kohn–Sham molecular orbitals calculated for PyBTM-(Me2Res). b) Chemical structures of the used materials in this work. c) Energy level diagram of the materials considering calculated electrochemical HOMO and LUMO levels. For PyBTM-(Me2Res) SOMO and SUMO levels are indicated with solid contour, while HOMO level is indicated with dashed contour. d) Device structure of r-OLET.

Table 1. Summary of the main figures of merit of r-OLETs.

PyBTM-(Me2Res) concentration	HIL	μ_e [a)] [$cm^2\ V^{-1}\ s^{-1}$]	V_{th} [a)] [V]	I_{DS} max[b)] [μA]	EL power max[b)] [nW]	EQE[b)] [%]	EML PLQY
0%	–	0.20	3.4	1050	–	–	–
5%	–	0.17	4.0	925	4	$2{\cdot}10^{-4}$	0.18
15%	–	0.10	4.8	580	22	$2{\cdot}10^{-3}$	0.15
15%	CBP	0.03	8.5	140	60	0.024 / 0.055[c)]	0.15
20%	–	0.06	2.3	370	15	$2{\cdot}10^{-3}$	0.12

[a)] calculated from saturation transfer curves in the saturation regime; [b)] at $V_{GS} = V_{DS} = 100$ V; [c)] best result.

$V^{-1}\ s^{-1}$ passing from guest-free to 20% of PyBTM-(Me2Res) in the EML. In contrast with the optical characterization that evidenced 5% as the optimal doping for maximizing PLQY, the EQE showed a significant enhancement of one order of magnitude, from $2{\cdot}10^{-4}$% to $2{\cdot}10^{-3}$%, when increasing the PyBTM-(Me2Res) content from 5% to 15% (Table 1). Moreover, by increasing the radical concentration from 5% to 15% the OLET emitted power showed a fivefold enhancement despite the PLQY of the EML decreased from 0.18 to 0.15, respectively. Eventually, 15% PyBTM-(Me2Res) resulted to be the best concentration in terms of maximization of EQE and optical power of emission of OLETs. The mismatch between the behavior of PLQY of the EML and device figures-of-merit (FOMs) as a function of the radical content suggests that under electrical excitation the host–guest energetics cannot be the only criteria to be considered for the exciton formation in r-OLETs.

Once selected the optimal PyBTM-(Me2Res) concentration at 15% in TPBi, we further boosted the OLET optical FOMs by integrating a hole injection layer (HIL) between EML and source and drain electrodes (Figure 1d). Even if the threshold gate voltage for electron had increased, the use of CBP as HIL led to a threefold enhancement of the optical power of the r-OLET, while the EQE increased from $2{\cdot}10^{-3}$% to 0.024%. The OLET efficiency was further enhanced by optimizing the gold/CBP interface to avoid detrimental diffusion of metal from the electrodes into the HIL,[62,63] and a best value of EQE % as high as 0.055% was obtained (Table 1). The optoelectronic characteristics of the resulting OLET are reported in **Figure 2**. Output curves (Figure 2a) show the electrical n-polarized operation of the device where linear and saturation regimes are clearly distinguishable. The saturation transfer curve at $V_{DS} = 100$ V (Figure 2b) exhibits the quadratic behavior expected for unipolar OLETs, with EL power increasing with the I_{DS} current (Figure S5, Supporting Information). The electroluminescence spectrum reported in Figure 2c confirms the emission from PyBTM-(Me2Res) peaked at 657 nm that matches the photoluminescence spectrum of the EML (Figure S3, Supporting Information). Interestingly, the contribution from TPBi emission at 385 nm was not observed in the EL spectrum, differently from what observed in the photoluminescence spectrum of the 15% blend when optically exciting the host.

Differently from what expected in the case of unipolar field-effect devices, the functional behavior of the optical power in output curves (Figure 2a) saturates after a linear increase only at low applied V_{GS}, while a continuous monotonic increase with increasing V_{DS} is observed for $V_{GS} \geq 40$ V. Moreover, the EL signal collected during the transfer characteristic (Figure 2b) displayed a double slope behavior as a function of the applied V_{GS} that cannot be described by the expected quadratic behavior of the collected I_{DS} (Figure S5, Supporting Information).[23] Finally, a non-negligible hysteresis is observed when passing from forward to backward V_{GS} scan of I_{DS}, with a prominent increase at around $V_{GS} = 80$ V. As we already demonstrated in ambipolar multilayer OLETs, the presence of a change of the slope and/or of a relative maximum in the EL signal at V_{DS} value at around $V_{GS}/2$ in saturation transfer characteristic is correlated to the merge of hole and electron density distributions within the transistor channel with consequent electroluminescence emission.[64] However, the optical image of the r-OLET in electrical ambipolar regime showed that radiative recombination is confined at the edge of drain electrode spreading for ≈10 μm toward the inner side of the electrode, as for unipolar OLETs (Figure 2d). In order to address the unexpected EL functional behavior in r-OLET, we fabricated a reference OLET (Figure S6, Supporting Information) with exactly the same architecture, only substituting PyBTM-(Me2Res) with 4-(dicyanomethylene)-2-methyl-6-(4-dimethylaminostyryl)-4*H*-pyran (DCM), a singlet closed-shell emitter that is typically used in energy-transfer host–guest EML in organic optoelectronic devices as in the case of OLETs.[64,65] As shown by both the I_{DS} and EL curves collected during saturation-transfer characteristics (Figure S6c, Supporting Information), reference singlet-emitter OLET can be considered a totally unipolar device where the efficiency of the process of formation of light in the EML is almost proportionally correlated to the number of majority carriers flowing in the transistor channel.

Evidently, in the case of using PyBTM-(Me2Res) molecules as emissive guests, other additive mechanisms can be considered in the exciton and, consequently, light formation processes,[66] that we investigated by means of time-resolved EL spectroscopy.[67,68] Measurements were carried out at fixed $V_{GS} = 100$ V by applying V_{DS} through periodic rectangular voltage pulses, with pulse height from 0 to 90 V and pulse width of 1μs at a repetition rate of 108 kHz. **Figure 3**a shows the transient EL signal recorded at 650 nm (i.e. at the maximum of the steady-state EL spectrum). The EL(t) signal increases within the voltage pulse and, at the pulse end, the EL intensity drops multi-exponentially in time. EL(λ) spectra were collected in four different time windows (Figure 3b), respectively within the V_{DS} pulse (W0), immediately after the V_{DS} pulse (W1), in a medium EL delay window (W2), and in further delayed EL region (W3) (Figure 3a,b).

The collected EL(λ) spectra show, in all the different time ranges, identical features, which are ascribed to the steady-state PL spectrum of PyBTM-(Me2Res). Therefore, a single emissive

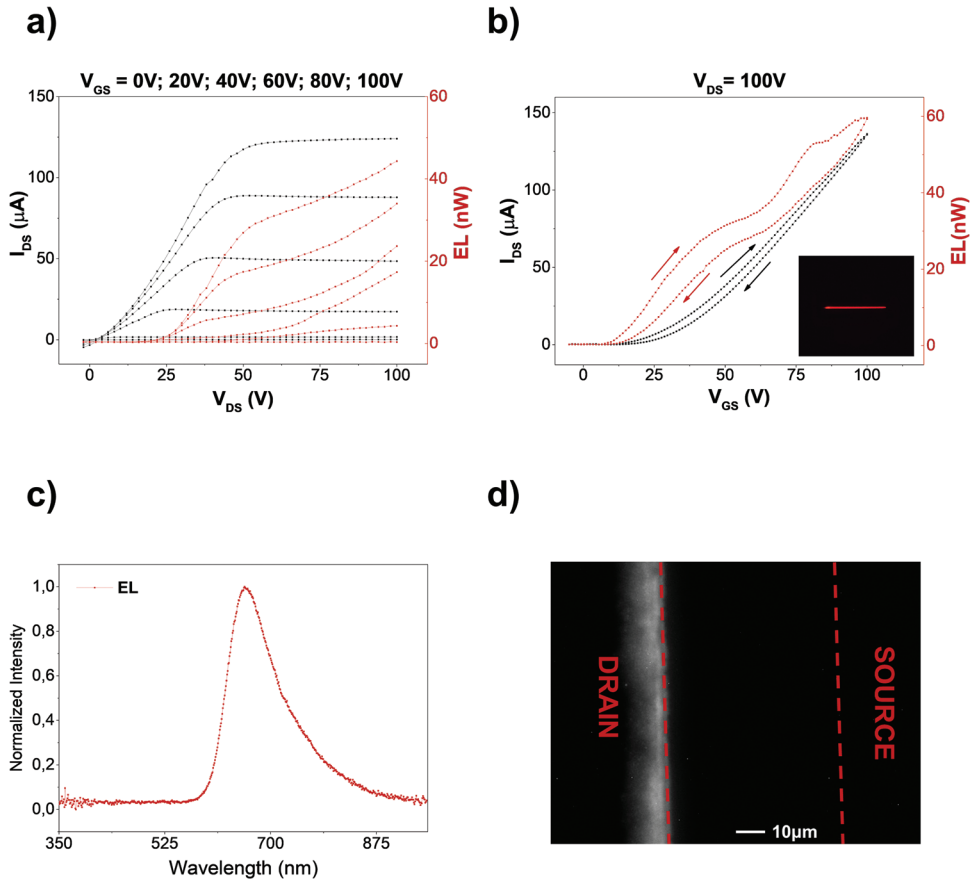

Figure 2. Radical-OLET characterization curves. a) Output curves recorded at V_{GS} ranging from 0 to 100 V at intervals of 20 V; b) n-type saturation transfer curve at V_{DS} = 100 V collected both in forward and backward scan (arrows indicate the direction of the scanning); in the inset a picture of the device switched on at V_{GS} = V_{DS} = 100 V is reported. c) Normalized electroluminescence spectrum of r-OLET. d) Optical image taken with 60x magnification objective of r-OLET biased at V_{GS} = 50 V and V_{DS} = 100 V, i.e. ideal ambipolar bias conditions.

state involving SUMO and HOMO levels of PyBTM-(Me2Res) is responsible for the exciton formation and then light emission from the device, excluding any possible relaxation into other lower-energy states. Accordingly, in transient EL(λ) spectra no TPBi contribution at λ = 385 nm can be observed even immediately after the V_{DS} pulse onset (Figure S7, Supporting Information). This observation is in agreement with the absence of TPBi spectral contribution in the steady-state EL spectrum reported in Figure 2c.

We interpolated the EL(t) signal by a tri-exponential decay obtaining an intensity-averaged decay time of 1.8 μs, that is dominated (63.1%) by the slow component (2.7 μs) (Table S3, Supporting Information). Since the PL decay time for PyBTM-like radicals in solution and solid state is tens of ns,[54] the decay in the order of microseconds in EL indicates that the exciton formation under electrical excitation involves slow processes that may correlate well with the presence of trapped charges at the radical sites.[69,70] Accordingly, an EL overshoot caused by trapped charges is recorded immediately after the end of the V_{DS} pulse (identified with a "*" in Figure 3a), as also reported for radical OLEDs dominated by charge trapping mechanism, while absent if good host-to-radical energy transfer is present.[42] Moreover, in the signal within the V_{DS} pulse, a strong modulation in EL is observed in the first 300 ns after the pulse offset. Time resolved EL(λ) spectra, as collected within the V_{DS} pulse every 200 ns (Figure 3a inset), confirm that the EL signal always originates from radiative recombination at radical sites. The observed EL modulation is likely caused by electrons still trapped from previously applied V_{DS} pulse that quickly recall holes from HIL when a new V_{DS} pulse is applied. Moreover, a long delay transient EL(t) measurement was carried out by changing the V_{DS} pulse width from 1 μs to 5 μs and consequently enlarging the observed time window from 5 to 50 μs (Figure 3c). The transient EL(t) profile is coherent with the one recorded in the shorter time interval: within the V_{DS} pulse the initial burst is still present, then the signal continuously increases in the 5 μs wide pulse. It has been reported that the presence of trapped charges in OLEDs increases the EL rise time within the voltage pulse,[70] so that the lack of saturation in EL signal in r-OLET upon increasing the width of the V_{DS} pulse indicates the presence of trapped electrons. Moreover, EL(λ) spectra collected in various long delay time windows (Figure 3d) further suggest that the only emissive state is ascribed to radical sites. Indeed, computational calculations showed that PyBTM-(Me2Res) has a strong ability to trap electrons. This is evidenced by a significant decrease in the SUMO orbital energy when an additional electron is present on the molecule, with the

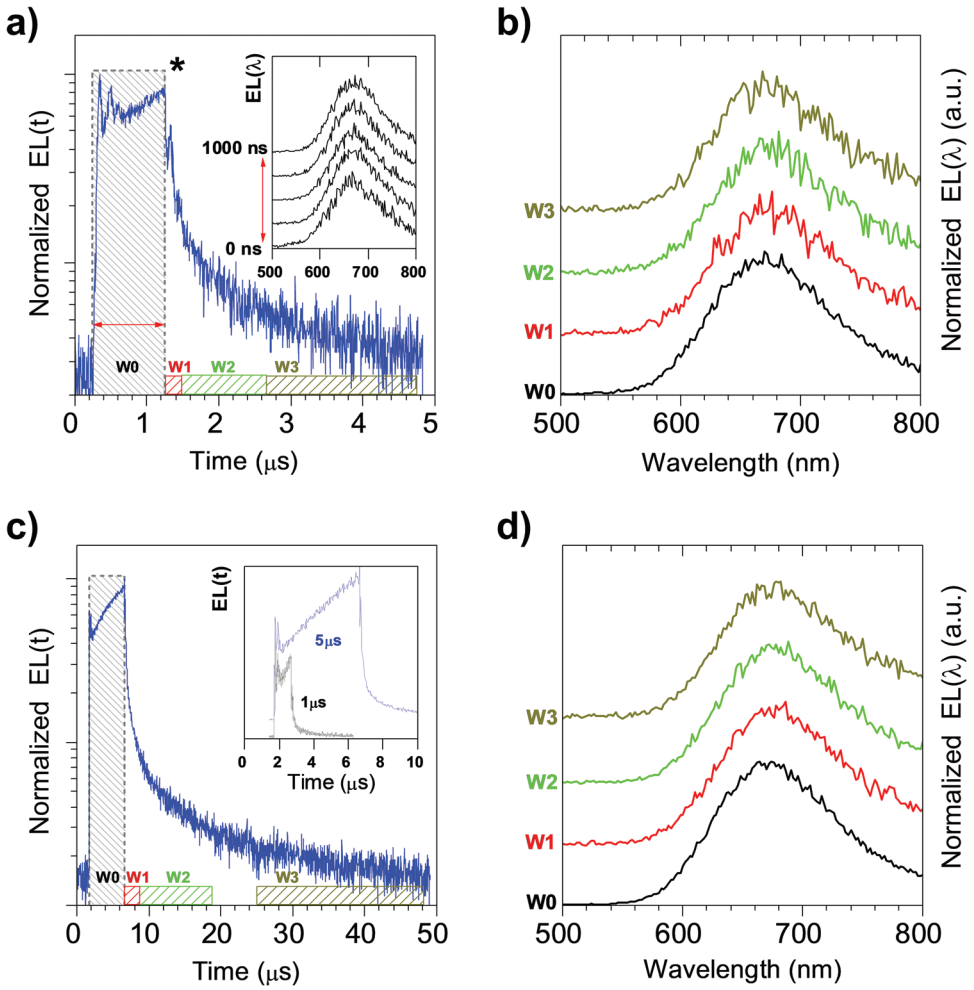

Figure 3. Transient electroluminescence EL(t) analysis of r-OLETs driven by a fixed V_{GS} = 100 V and by a pulsed V_{DS} = 90 V. a) normalized semi-log plot of EL(t) (blue trace), in a 5 μs time range, as measured at λ = 650 nm by applying rectangular voltage pulses of V_{DS} (pulse width = 1000 ns, gray-shaded), at 108 kHz repetition rate. a.inset) Time evolution of EL spectrum (λ = 500 nm – 800 nm) during the application of the voltage pulse, between t = 0 ns and t = 1000 ns, every 200 ns. The normalized spectra are vertically shifted for sake of clarity. The "*" identifies the EL afterpeak. b) Normalized EL spectra collected within various time intervals (time-windows extension of Δt ns) indicated as W0,...,W3 in a), during and after the application of the V_{DS} voltage pulse (W0: Δt = 1000 ns within the pulse, W1: Δt = 220 ns after pulse end (a.p.e.), W2: Δt = 1200 ns, from 220 ns to 1420 a.p.e, W3: Δt = 2100 ns, from 2450 ns to 4550 a.p.e). c) EL(t) at λ = 650 nm, in a 50 μs time range, with pulsed V_{DS} (pulsewidth = 5 μs, gray-shaded), at 10 kHz repetition rate. c.inset) Comparison of EL(t) at the two pulsewidths (linear plot, decays normalized at the EL onset values and vertically shifted). d) Normalized EL spectra within time-windows (W0, ..., W3 in c), (W0: Δt = 5 μs within the pulse, W1: Δt = 2 μs a.p.e), W2: Δt = 10 μs, from 2 μs to 12 μs a.p.e, W3: Δt = 25 μs, from 20 μs to 45 μs a.p.e).

energy dropping from −3.50 eV (unoccupied β-SUMO orbital) (Table S1, Supporting Information) to −4.05 eV (E[0/-] reduction potential) (Figure 1c). Accordingly, a two-step process in exciton generation can be assumed, where the neutral radical is first reduced to the corresponding closed shell anion that subsequently recalls a hole to form the emissive doublet excited state (Figure S8, Supporting Information).

To note, a surprisingly long-lived emission was still well detectable at 40 μs after the end of the V_{DS} pulse (Figure 3d, W3). Transient EL(t) fitting by a tri-exponential decay results in an intensity averaged time decay of 8.8 μs, with a significant slow decay component of ≈13.2 μs that contributes for more than 63% (Table S3, Supporting Information). This emission duration is fully matching the requirements for afterglow applications.[71] The presence of long-lasting EL is a promising characteristic of r-OLETs for their use in long-persistent luminescent systems.

Once demonstrated the charge trapping mechanism in r-OLET, we focused on the role of the density of trapped electrons in the EML by probing the entire set of operational conditions of the devices in terms of V_{GS} and V_{DS} applied bias to map the collected I_{DS} (**Figure 4a**) and EL signals (Figure 4b). The voltage ranges of V_{GS} and V_{DS} were also increased to 130 V and V_{GS} was scanned both in forward and backward directions to obtain a comprehensive description of the device working. The maps were obtained collecting the r-OLET response during 65 consecutive transfer curves varying the V_{DS} bias, and eight representative EL curves are reported in Figure S9 (Supporting Information). In the 2D intensity map of I_{DS}, the bias condition at which

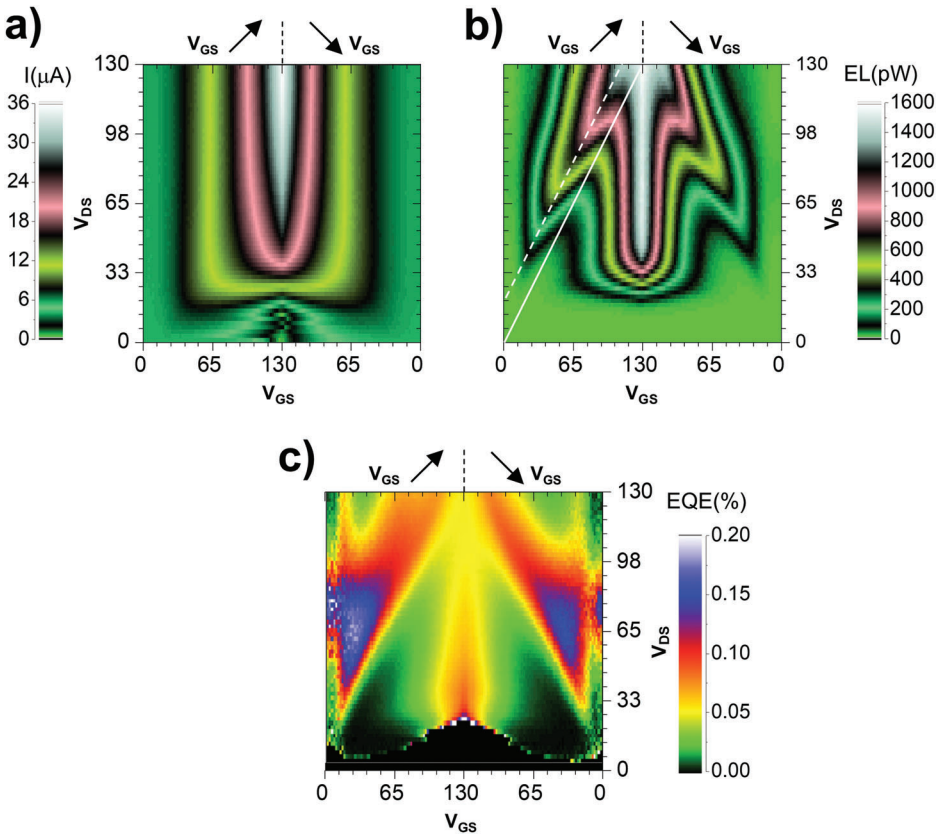

Figure 4. r-OLET 2D intensity maps as a function of V_{GS} and V_{DS} bias, during both forward and backward V_{GS} scan, of a) I_{DS} current; b) electroluminescence (EL) power map collected at $\lambda = 650$ nm; as a guide for the eye: white lines highlight the bias at which $V_{GS} = V_{DS}$ (solid line) and $V_{GS} = V_{DS} - 20$ V (dashed line); c) EQE %. (see text for details).

the device enters in saturation regime, i.e. by increasing V_{DS} bias at fixed V_{GS} bias, is indicated by equal color related to a constant I_{DS} value (Figure 4a). Observing the EL map (Figure 4b), the overall EL pattern is completely different from that of I_{DS}, matching the latter only when $V_{DS} < V_{GS}$, with a quasi-rectangular shape. The continuous straight red line corresponding to $V_{GS} = V_{DS}$ is a guide for the eyes to discriminate the different bias regions. In this region the EL functional behavior is proportional to the flowing I_{DS} as for unipolar OLETs. A different functional behavior with respect to the I_{DS} map is instead visible in the region of $V_{DS} > V_{GS}$ and $V_{GS} > V_{th}$, where an enhancement of EL is observed by increasing V_{DS} bias (at fixed V_{GS} bias) even if I_{DS} saturates. This behavior is in fact in agreement with the already observed lack of EL saturation in output curves (Figure 2a). Interestingly, this operational condition ($V_{DS} > V_{GS}$ and $V_{GS} > V_{th}$) is the one that allows the formation of two opposite charge accumulation layers in the case of ideal ambipolar FETs under positive polarization, i.e. electron-transport operation.[72,73] Thus, the formation of a hole accumulation region could be advocated to justify the collected EL signal: however, no contribution to the collected I_{DS} can be attributed to a purely hole current in the device channel since no hole-transporting OSC is present in the device. By considering the mechanisms of EL formation previously derived from the EL transient measurement, we may infer that exciton formation is efficiently enabled in a voltage bias region where the electron channel is not completely filled (thus not in saturation bias conditions as expected) because of the long-lasting electron trapping in radical sites in the EML. In turn, an as-formed non-negligible negative space charge density in the EML promotes the injection and drift of positive charges (i.e. holes) from the HIL which then recombine radiatively when trapped in the radical sites. In particular, it can be observed that this ambipolar-like behavior where EL signal is locally maximized is always obtained at $V_{GS} = V_{DS} - 20$ V being $V_{GS} > V_{th}$ (Figure 4b dashed red line), thus −20 V can be considered as the potential difference between the EML and HIL that generates a transversal electric field in the active region of the r-OLET responsible for the injection of minority charge carriers leading to an improved exciton formation.

Accordingly, a 2D map of EQE was calculated (Figure 4c) as the point-to-point ratio between the EL and the I_{DS} map. As conceivable, the features of the EQE map are similar to those of the EL map, and different operative regions can be distinguished. It can be easily observed that the optical efficiency of the device is higher in the ambipolar-like region rather than in the unipolar one (blue regions vs the red-yellow region around $V_{GS} = V_{DS} = 130$ V). In fact, it is clear from the EQE map that the maximum EQE value of 0.2% is recorded at $V_{GS} = 28$ V and $V_{DS} = 60$ V, satisfying the theoretical ambipolar condition.[72] Specifically, the applied V_{GS} is higher than the threshold gate voltage for electrons (8.5 V), and the difference between V_{GS} and V_{DS} is lower than the supposed threshold gate voltage for holes (−20 V).[74] We remark that this value of EQE is almost an order of magnitude higher

than the value obtained for standard optoelectronic characterization of unipolar devices reported in Table 1.

Further considerations on the working mechanisms of r-OLETs can be drawn by analysing the ratio of the number of exciton formation events within the device with respect to the number of charges flowing in the device. Typically, this parameter (namely γ) is a factor in the analytical expression of the EQE that is defined as it follows:[75]

$$EQE = \eta_{out} \times \varphi_{PLQY} \times \gamma \times \eta_{spin} \quad (1)$$

where η_{out} is the light outcoupling efficiency, from the device into the open space, φ_{PLQY} is the photoluminescence quantum yield of the EML, and η_{spin} is spin multiplicity of the radiatively recombining excitons. While φ_{PLQY} and η_{spin} only depend on the photophysical properties of the emissive sites in the EML, and η_{out} depends on the optical characteristics of used materials and architecture of the device,[64,75–77] γ is the only factor that depends on the operative bias conditions. Therefore, we first estimated γ for our r-OLETs in the unipolar region (i.e. $V_{DS} = V_{GS} = 100$ V) obtaining a value (1.8%) that is comparable with the one calculated for the purely unipolar OLET with DCM as emitter (1.5%) (γ calculations are reported in Supporting Information and data are summarized in Table S4, Supporting Information). However, moving from the unipolar region to the more efficient ambipolar-like one, γ value of the r-OLETs increases reaching a value as high as 7% at maximum EQE (i.e. $V_{GS} = 28$ V and $V_{DS} = 60$ V), that is up to threefold higher than the maximum γ value for the reference DCM-based OLET (2.3%). In the end, the use of radical emitters may represent a strategy to effectively increase the EQE in unipolar OLETs by combining two effects: first, the intrinsic increase in the overcoming the spin statistic limitations of singlet organic emitters and representing a cost-effective alternative to triplet organometallic emitters; second, to tackle the typical poor balance between major and minor charge carriers in unipolar OLETs, due to their capability of building up a long-living space charge density within the EML.

3. Conclusion

In conclusion, a unipolar n-type transistor architecture was designed and validated to house radical emitters, i.e. PyBTM-like open shell molecules, opening the way to exploit electroluminescence from doublet states in OLETs. The mismatch between PL properties and the emissive characteristics in whole r-OLETs of host–guest emissive systems at different radical content suggested a charge-trapping dominated exciton-formation mechanism, supported by DFT calculations, when the system is electrically biased. The assumption was indeed demonstrated by transient-EL measurements applying rectangular source-drain voltage pulses and analyzing the signal decay in two different time ranges, i.e. 5 and 50 µs. Surprisingly, long-persistent EL up to 40 µs after the voltage removal due to trapped charges at radical sites was reported, highlighting the use of r-OLETs for afterglow applications. We inferred that trapped electrons in the radical sites built a negative space charge density in the EML, promoting the injection and diffusion of holes from HIL, paving the possibility to exploit charge trapping mechanism in exciton generation. Consequently, a threefold enhancement of the balance of opposite charge carriers with respect to a commonly used singlet emitter, i.e. DCM, was reported when the device is biased in a more efficient ambipolar-like working condition. In this view, the advantage in employing radical as emitters in OLETs, lies not only in the exploitation of more efficient spin doublet excitons, but also in the ability of radicals to act as electron traps, as demonstrated for PyBTM-(Me2Res), to fully exploit the electrical configuration of a transistor by acting on V_{GS} to balance the charge density, which is impossible in diode architectures where charge trapping is generally considered detrimental.

4. Experimental Section

Synthesis of PyBTM-(Me2Res): Materials: all reagents and solvents were purchased from Acros, Fisher Scientific and BLDpharm. The two-step reaction scheme is reported in Scheme S1 (Supporting Information).

PyBTM-H was synthesized according to published procedures.[54]

*Step 1 – Synthesis of **PyBTM-(Me2Res)-H***: In a 50 mL, two necked round-bottom flask equipped with a condenser, **PyBTM-H** (782 mg, 1.50 mmol), 2,6-dimethoxyphenylboronic acid (1.371 g, 7.534 mmol), Pd(dtbpf)Cl_2 (78.0 mg, 0.120 mmol) and Kolliphor EL (107 mg) were put under nitrogen atmosphere. Degassed water (5.4 mL) and toluene (0.6 mL) were added, and the mixture was allowed to stir vigorously at 80 °C for 5 min before addition of Et_3N (2.1 mL, 15 mmol). The reaction mixture was kept at 80 °C for 17 h, then cooled down to room temperature, and the solvents were removed under reduced pressure. Toluene was added to the crude, and the mixture dried over Na_2SO_4 and filtered. The obtained solution was purified by gradient column chromatography (eluent: toluene to toluene/DCM 95:5) to afford 357 mg of **PyBTM-(Me2Res)-H** as a white powder (0.573 mmol, 38.2% yield). Rf (toluene) = 0.28.

NMR spectra are reported in Figures S10–S13 (Supporting Information).

^{1}H NMR ($CDCl_3$, 400 MHz): δ 8.50 (s, 1H), 8.48 (s, 1H), 8.37 (s, 1H), 8.36 (s, 1H), 7.41 (d, J = 2.2 Hz, 1H), 7.38 (d, J = 2.2 Hz, 1H), 7.36 (d, J = 1.7 Hz, 1H), 7.34 (d, J = 1.7 Hz, 1H), 7.31-7.26 (m, 3H), 7.24 (d, J = 2.2 Hz, 1H), 7.23 (d, J = 1.7 Hz, 1H), 7.20 (d, J = 1.7 Hz, 1H), 6.813 (s, 1H), 6.807 (s, 1H), 6.63 (m, 2H), 6.61 (m,2H), 3.74 (m, 12H) ppm

^{13}C NMR ($CDCl_3$, 101 MHz): δ 157.43, 149.48, 149.24, 147.65, 147.53, 144.31, 144.22, 138.33, 137.86, 137.50, 137.19, 136.09, 136.06, 136.04, 135.98, 135.49, 135.48, 134.79, 134.45, 133.83, 133.73, 133.53, 133.42, 132.91, 132.60, 131.47, 131.18, 131.14, 130.99, 130.23, 129.73, 128.52, 128.24, 116.19, 116.17, 104.18, 55.94, 49.91 ppm

*Step 2 – Synthesis of **PyBTM-(Me2Res)***: In a 50 mL roundbottom flask, **PyBTM-(Me2Res)-H** (150 mg, 0.241 mmol) and ^{t}BuOK (98 mg, 0.87 mmol) are put under nitrogen atmosphere, then anhydrous THF (5,0 mL) is added. The reaction is stirred in the dark at room temperature for four hours. In a 25 mL roundbottom flask, a solution of I_2 (355 mg, 1.40 mmol) in anhydrous Et_2O (3.0 mL) under nitrogen atmosphere is prepared, and subsequently added to the first solution. The reaction mixture is stirred for 18 h, then the solvent is evaporated and the crude is purified by filtration over a pad of silica using Et_2O as the eluent. After solvent evaporation, the product is recovered as a black powder (136 mg, 0.219 mmol, 90.8% yield).

HRMS (MALDI-TOF MS) *m/z*: $[M-H]^-$ calculated for $C_{26}H_{15}C_7NO_2^-$ 619.8899; found 619.8949.

DFT Simulations: Atomistic simulations of PyBTM-(Me2Res), P13, TPBi and CBP have been carried out using a multi-level protocol. The most stable conformers of the molecules have been individuated by a conformer-rotamer ensemble sampling tool (CREST) algorithm,[78] which uses the GFN2-xTB tight-binding Hamiltonian as "engine" for the search of minimum energy configurations.[79,80] Then, electronic and optical properties of the molecules have been investigated using (time-dependent) density functional theory simulations, performed in a GTO framework by using the ORCA suite of programs.[81,82] In detail, the Kohn-Sham orbitals have been expanded on an all-electron def2-TZVPP

Gaussian-type basis set.[83,84] The corresponding def2/J basis has been also used as an auxiliary basis set for Coulomb fitting in a resolution-of-identity/chain-of-spheres (RIJCOSX) framework. Molecular geometries have been fully optimized and their properties investigated by using the B3LYP functional,[85] with the addition of the pairwise D3 correction for the calculation of dispersion forces.[86] The absorption and emission vibronic spectra of PyBTM-(Me2Res) have been calculated using time-dependent density functional theory at the same B3LYP@def2-TZVPP level of theory, in the framework of the excited state module (ESD) implemented in ORCA.[87] A large basis of 600 vectors connecting occupied and unoccupied Kohn–Sham orbitals has been used to build the Davidson expansion space for the calculations of the first 30 electronic transitions of all the molecules. Finally, redox potentials of all the molecules have been calculated using the M06-2X hybrid functional[88] and the def2-TZVPP basis set. The molecules and their positive and negative ions have been embedded in an implicit CH_2Cl_2 solvent using a conductor-like polarizable continuum model (CPCM)[89] to calculate electronic and solvation energies. Thermochemical properties of the same molecules have been calculated using the B3LYP functional introduced above. Redox potentials have been calculated as ΔG values between neutral and charged species as follow:

$$\Delta G_{R/0} = \Delta \text{Uel (m062x@tzvpp)} + \Delta \text{ZPE (b3lyp@svp)} + \Delta G_{\text{trans,rot,vib-TS}} \text{ (b3lyp@svp)} \quad (2)$$

where ΔUel(m062x@tzvpp) is the difference of internal electronic energy calculated at m06-2x@def2-tzvpp level of theory. ΔZPE(b3lyp@svp) and $\Delta G_{\text{trans,rot,vib-TS}}$(b3lyp@svp) are, respectively, the contribution of zero-point energy and thermal free energy both calculated at b3lyp@svp level of theory.

Devices Fabrication: All the devices were fabricated in bottom-gate/top-contact configuration on 25mm × 25mm transparent glass/ITO substrates. 450 nm thick PMMA layer was deposited by spin-coating as gate dielectric in according to the literature procedure.[60] Radical-OLETs structure were composed of i) 40 nm of n-type semiconductor P13 (Sigma–Aldrich) sublimed at 0.1 Å sec^{-1} ii) 60 nm thick host–guest EML of TPBi (Ossila) (host) and PyBTM-(Me2Res) (guest) at different concentrations, i.e. 5%, 15%, and 20%, sublimed maintaining the guest deposition rate constant at 0.1 Å sec^{-1} while decreasing the deposition rate of the host from 2 to 0.6 to 0.5 Å sec^{-1}, respectively. The HIL consisted of 15 nm of CBP (American Dye Source, Inc.) sublimed at 0.1 Å sec^{-1}. The organic stack was covered by 80 nm thick gold source and drain electrodes deposited by thermal evaporation at 0.5 Å sec^{-1}. For the optimized radical-OLET, gold deposition rate was decreased down to 0.1 Å sec^{-1}. Reference OLET was fabricated substituting PyBTM-(Me2Res) with DCM (Sigma–Aldrich) maintaining the same concentration of radical guest in TPBi, i.e. 15%. Both the organic layers and the metal electrodes were deposited using shadow masks in a homemade high-vacuum deposition chamber at a base pressure of 10^{-7} mbar. The resulting devices presented the following geometrical characteristics: 70 µm channel length (L), 12 mm channel width (W) and 500 µm wide source and drain electrodes.

Optoelectronic Characterization of OLETs: The electrical and optical measurements of OLETs were performed in an inert atmosphere inside a nitrogen-filled glovebox using a standard SUSS probe station coupled to a B1500A Agilent semiconductor device analyzer. The light output was measured at the bottom side of the substrates with a silicon photodiode (a sensitivity of 0.38 A W^{-1} at 600 nm) directly in contact with the devices. OLET steady state EL spectrum was obtained collecting the signal with a Hamamatsu PMA optical multichannel analyzer. The field-effect mobility in the saturation regime (µ) was calculated using the equation $I_{DS} = (W/2L)C_i\mu(V_{GS} - V_{Th})^2$, where C_i is the capacitance per unit area of the insulating layer and V_{Th} is the threshold voltage extracted from the square root of the drain current ($I_{DS}^{1/2}$) versus gate voltage (V_{GS}) characteristics.

Photoluminescence Measurements: The UV–vis absorption spectra of TPBi and PyBTM-(Me2Res) solutions were obtained with a Jasco V-550 UV/Vis spectrophotometer, while the PL spectra were obtained with a Hamamatsu PMA optical multichannel analyzer by optically exciting the samples at proper wavelengths, i.e. 325 nm for TPBi and 375 nm for PyBTM-(Me2Res). The steady state PL spectra of different EMLs on quartz substrates were obtained with the Hamamatsu PMA optical multichannel analyzer by optically exciting the samples at 325 nm accordingly to the absorption spectra of the host (TPBi). The PLQY measurements were obtained with a FS5-SS Hamamatsu steady state spectrometer with the correlated integrating sphere module.

Optical Imaging: Optical imaging of the encapsulated OLET was recorded with a Nikon Eclipse 2000-E microscope using 60x magnification objective and a Hamamatsu high-resolution digital camera coupled to a B1500A Agilent semiconductor device analyzer to drive the device.

Time-Resolved EL Measurements: In time-resolved EL measurements OLET V_{GS} was biased by a Keithley 2400 SMU at a fixed voltage, whereas an Agilent 8114A generator was used for applying pulsed V_{DS} bias. The output low of both sources was common grounded. Two V_{DS} pulse widths were applied, i.e. 1 and 5 µs, whereas the pulse repetition rates were 108 and 10 kHz, respectively. Photons emitted from the device were collected using an f/4, 300 mm, Acton Research Spectra Pro SP-2300i triple-turret monochromator with a Hamamatsu H7422-20 Peltier-cooled photosensor module as the detector. EL transients were measured by means of PicoQuant TimeHarp-100 and PicoQuant NanoHarp-250 electronic boards synchronously driven by the pulse generator.

OLET 2D Maps: I_{DS} (V_{DS}, V_{GS}) and EL(V_{DS},V_{GS}) 2D maps were obtained biasing the OLET by two Keithley 2400 SMU in common ground. Optical and electrical signals were collected by performing subsequent transfer curves scanning V_{GS} ($\Delta V_{GS} = 2$ V) from 0 to 130 V and back to 0 V keeping fixed V_{DS}. V_{DS} was then incremented every cycle from 0 to 130 V with $\Delta V_{DS} = 2$ V. OLET's electroluminescence (detection $\lambda = 650$ nm) was collected by using the same optical setup used for transient EL measurements using an integration time $\Delta t = 1$ s for every point of the map. The OLET output optical power was calculated using a NIST calibrated silicon photodiode (sensitivity of 0.38 A W^{-1} at 600 nm) as reference. EQE 2D map was calculated starting from EL (V_{DS}, V_{GS}) and I_{DS} (V_{DS}, V_{GS}) maps.

Supporting Information

Supporting Information is available from the Wiley Online Library or from the author.

Acknowledgements

The authors thank Federico Prescimone, Vincenzo Ragona, and Tiziano Bonfiglioli for the technical support and Dr. Alessio Mezzi for the valuable scientific discussions. This work received funding from the European Union's Horizon 2020 research and innovation program under grant agreement no. 101016706 (h-ALO) and has been supported by the project "MULTIRADICALS4LIGHT: Design, synthesis, and characterization of inert MULTIfunctional diRADICALoidS for organic LIGHT-emitting transistors" funded by the MIUR Progetti di Ricerca di Rilevante Interesse Nazionale (PRIN) – 202253P3YJ_PE5_PRIN2022.

Open access publishing facilitated by Consiglio Nazionale delle Ricerche, as part of the Wiley - CRUI-CARE agreement.

Conflict of Interest

The authors declare no conflict of interest.

Data Availability Statement

The data that support the findings of this study are available from the corresponding author upon reasonable request.

Keywords

ambipolar-like operation, charge trapping, external quantum efficiency, organic light-emitting transistors, organic radical emitters, transient electroluminescence

Received: July 5, 2024
Revised: September 17, 2024
Published online:

[1] C. Zhang, P. Chen, W. Hu, *Small* **2016**, *12*, 1252.
[2] J. Zaumseil, *Adv. Funct. Mater.* **2020**, *30*, 1905269.
[3] Z. Qin, H. Gao, H. Dong, W. Hu, *Adv. Mater.* **2021**, *33*, 2007149.
[4] M. U. Chaudhry, K. Muhieddine, R. Wawrzinek, J. Sobus, K. Tandy, S. C. Lo, E. B. Namdas, *Adv. Funct. Mater.* **2020**, *30*, 1905282.
[5] M. Prosa, E. Benvenuti, D. Kallweit, P. Pellacani, M. Toerker, M. Bolognesi, L. Lopez-Sanchez, V. Ragona, F. Marabelli, S. Toffanin, *Adv. Funct. Mater.* **2021**, *31*, 2104927.
[6] G. Gelinck, P. Heremans, K. Nomoto, T. D. Anthopoulos, *Adv. Mater.* **2010**, *22*, 3778.
[7] H. Sirringhaus, *Adv. Mater.* **2014**, *26*, 1319.
[8] M. Prosa, M. Bolognesi, L. Fornasari, G. Grasso, L. Lopez-Sanchez, F. Marabelli, S. Toffanin, *Nanomaterials* **2020**, *10*, 480.
[9] M. Muccini, W. Koopman, S. Toffanin, *Laser Photon Rev.* **2012**, *6*, 258.
[10] S. Toffanin, V. Benfenati, A. Pistone, S. Bonetti, W. Koopman, T. Posati, A. Sagnella, M. Natali, R. Zamboni, G. Ruani, M. Muccini, *J. Mater. Chem. B.* **2013**, *1*, 3850.
[11] M. Prosa, S. Moschetto, E. Benvenuti, M. Zambianchi, M. Muccini, M. Melucci, S. Toffanin, *J. Mater. Chem C Mater.* **2020**, *8*, 15048.
[12] W. W. A. Koopman, S. Toffanin, M. Natali, S. Troisi, R. Capelli, V. Biondo, A. Stefani, M. Muccini, *Nano Lett.* **2014**, *14*, 1695.
[13] S. Moschetto, E. Benvenuti, H. Usta, R. Ozdemir, A. Facchetti, M. Muccini, M. Prosa, S. Toffanin, *Adv. Mater. Interfaces* **2022**, *9*, 2101926.
[14] M. Durso, C. Bettini, A. Zanelli, M. Gazzano, M. G. Lobello, F. De Angelis, V. Biondo, D. Gentili, R. Capelli, M. Cavallini, S. Toffanin, M. Muccini, M. Melucci, *Org. Electron.* **2013**, *14*, 3089.
[15] H. Chen, W. Huang, T. J. Marks, A. Facchetti, H. Meng, *Small* **2021**, *17*, 2007661.
[16] Z. Miao, C. Gao, H. Gao, Z. Qin, W. Hu, H. Dong, *Adv. Mater.* **2024**, *36*, 2306725.
[17] Y. Chen, H. Wang, Y. Yao, Y. Wang, C. Ma, P. Samorì, *Adv. Mater.* **2021**, *33*, 2103369.
[18] W. S. C. Roelofs, W. H. Adriaans, R. A. J. Janssen, M. Kemerink, D. M. De Leeuw, *Adv. Funct. Mater.* **2013**, *23*, 4133.
[19] Y. Hu, L. Song, S. T. Zhang, Y. Lv, J. Lin, X. Guo, X. Liu, *Adv. Mater. Interfaces* **2020**, *7*, 2000657.
[20] M. Prosa, E. Benvenuti, M. Pasini, U. Giovanella, M. Bolognesi, L. Meazza, F. Galeotti, M. Muccini, S. Toffanin, *ACS Appl. Mater. Interfaces* **2018**, *10*, 25580.
[21] E. J. Feldmeier, M. Schidleja, C. Melzer, H. Von Seggern, *Adv. Mater.* **2010**, *22*, 3568.
[22] C. Soldano, R. D'Alpaos, G. Generali, *ACS Photonics* **2017**, *4*, 800.
[23] M. Muccini, S. Toffanin, *Organic Light-Emitting Transistors: Towards the Next Generation Display Technology*, John Wiley & Sons, New York **2016**.
[24] X. Ai, E. W. Evans, S. Dong, A. J. Gillett, H. Guo, Y. Chen, T. J. H. Hele, R. H. Friend, F. Li, *Nature* **2018**, *563*, 536.
[25] J. M. Hudson, T. J. H. Hele, E. W. Evans, *J. Appl. Phys.* **2021**, *129*, 180901.
[26] Q. Peng, A. Obolda, M. Zhang, F. Li, *Angew. Chem.– Int. Ed.* **2015**, *54*, 7091.
[27] Y. Hattori, T. Kusamoto, H. Nishihara, *Angew. Chem.* **2014**, *126*, 12039.
[28] S. Kimura, A. Tanushi, T. Kusamoto, S. Kochi, T. Sato, H. Nishihara, *Chem. Sci.* **2018**, *9*, 1996.
[29] K. Kato, S. Kimura, T. Kusamoto, H. Nishihara, Y. Teki, *Angew. Chem.* **2019**, *131*, 2632.
[30] Y. Hattori, R. Kitajima, W. Ota, R. Matsuoka, T. Kusamoto, T. Sato, K. Uchida, *Chem. Sci.* **2022**, *13*, 13418.
[31] L. Chen, M. Arnold, Y. Kittel, R. Blinder, F. Jelezko, A. J. C. Kuehne, *Adv. Opt. Mater.* **2022**, *10*, 2102101.
[32] S. Dong, A. Obolda, Q. Peng, Y. Zhang, S. Marder, F. Li, *Mater. Chem. Front* **2017**, *1*, 2132.
[33] H. Guo, Q. Peng, X. K. Chen, Q. Gu, S. Dong, E. W. Evans, A. J. Gillett, X. Ai, M. Zhang, D. Credgington, V. Coropceanu, R. H. Friend, J. L. Brédas, F. Li, *Nat. Mater.* **2019**, *18*, 977.
[34] A. Tanushi, S. Kimura, T. Kusamoto, M. Tominaga, Y. Kitagawa, M. Nakano, H. Nishihara, *J. Phys. Chem. C.* **2019**, *123*, 4417.
[35] Z. Cui, S. Ye, L. Wang, H. Guo, A. Obolda, S. Dong, Y. Chen, X. Ai, A. Abdurahman, M. Zhang, L. Wang, F. Li, *J. Phys. Chem. Lett.* **2018**, *9*, 6644.
[36] A. Abdurahman, T. J. H. Hele, Q. Gu, J. Zhang, Q. Peng, M. Zhang, R. H. Friend, F. Li, E. W. Evans, *Nat. Mater.* **2020**, *19*, 1224.
[37] H. H. Cho, S. Kimura, N. C. Greenham, Y. Tani, R. Matsuoka, H. Nishihara, R. H. Friend, T. Kusamoto, E. W. Evans, *Adv. Opt. Mater.* **2022**, *10*, 2200628.
[38] F. Li, A. J. Gillett, Q. Gu, J. Ding, Z. Chen, T. J. H. Hele, W. K. Myers, R. H. Friend, E. W. Evans, *Nat. Commun.* **2022**, *13*, 2744.
[39] Z. Cui, A. Abdurahman, X. Ai, F. Li, *CCS Chem.* **2020**, *2*, 1129.
[40] A. Obolda, X. Ai, M. Zhang, F. Li, *ACS Appl. Mater. Interfaces* **2016**, *8*, 35472.
[41] Y. Gao, A. Obolda, M. Zhang, F. Li, *Dyes Pigm.* **2017**, *139*, 644.
[42] H. H. Cho, S. Gorgon, H. C. Hung, J. Y. Huang, Y. R. Wu, F. Li, N. C. Greenham, E. W. Evans, R. H. Friend, *Adv. Mater.* **2023**, *35*, 2303666.
[43] C. He, Z. Li, Y. Lei, W. Zou, B. Suo, *J. Phys. Chem. Lett.* **2019**, *10*, 574.
[44] O. Sachnik, X. Tan, D. Dou, C. Haese, N. Kinaret, K. H. Lin, D. Andrienko, M. Baumgarten, R. Graf, G. J. A. H. Wetzelaer, J. J. Michels, P. W. M. Blom, *Nat. Mater.* **2023**, *22*, 1114.
[45] C. Santato, R. Capelli, M. A. Loi, M. Murgia, F. Cicoira, V. A. L. Roy, P. Stallinga, R. Zamboni, C. Rost, S. F. Karg, M. Muccini, *Synth. Met.* **2004**, *146*, 329.
[46] E. Cho, V. Coropceanu, J. L. Brédas, *J. Am. Chem. Soc.* **2020**, *142*, 17782.
[47] H. Chen, X. Xing, J. Miao, C. Zhao, M. Zhu, J. W. Bai, Y. He, H. Meng, *Adv. Opt. Mater.* **2020**, *8*, 1901651.
[48] K. Muhieddine, M. Ullah, B. N. Pal, P. Burn, E. B. Namdas, *Adv. Mater.* **2014**, *26*, 6410.
[49] P. He, C. Jiang, L. Lan, S. Sun, Y. Li, P. Gao, P. Zhang, X. Dai, J. Wang, J. Peng, Y. Cao, *ACS Nano* **2018**, *12*, 4624.
[50] M. Ullah, Y. H. Lin, K. Muhieddine, S. C. Lo, T. D. Anthopoulos, E. B. Namdas, *Adv. Opt. Mater.* **2016**, *4*, 231.
[51] J. Sobus, F. Bencheikh, M. Mamada, R. Wawrzinek, J. C. Ribierre, C. Adachi, S. C. Lo, E. B. Namdas, *Adv. Funct. Mater.* **2018**, *28*, 1800340.
[52] J. E. Anthony, A. Facchetti, M. Heeney, S. R. Marder, X. Zhan, *Adv. Mater.* **2010**, *22*, 3876.
[53] K. Muhieddine, M. Ullah, F. Maasoumi, P. L. Burn, E. B. Namdas, *Adv. Mater.* **2015**, *27*, 6677.
[54] S. Mattiello, F. Corsini, S. Mecca, M. Sassi, R. Ruffo, G. Mattioli, Y. Hattori, T. Kusamoto, G. Griffini, L. Beverina, *Mater. Adv.* **2021**, *2*, 7369.
[55] S. Mattiello, Y. Hattori, R. Kitajima, R. Matsuoka, T. Kusamoto, K. Uchida, L. Beverina, *J. Mater. Chem C. Mater.* **2022**, *10*, 15028.
[56] Q. Gu, A. Abdurahman, R. H. Friend, F. Li, *J. Phys. Chem. Lett.* **2020**, *11*, 5638.
[57] G. Mattioli, S. Mattiello, M. Sassi, L. Beverina, *J. Phys. Chem. C* **2020**, *124*, 3601.

[58] M. Natali, M. Prosa, A. Longo, M. Brucale, F. Mercuri, M. Buonomo, N. Lago, E. Benvenuti, F. Prescimone, C. Bettini, A. Cester, M. Melucci, M. Muccini, S. Toffanin, *ACS Appl. Mater. Interfaces* **2020**, *12*, 30616.
[59] L. Ma, D. Qin, Y. Liu, X. Zhan, *J Mater Chem C. Mater* **2018**, *6*, 535.
[60] M. Zambianchi, E. Benvenuti, C. Bettini, C. Zanardi, R. Seeber, D. Gentili, M. Cavallini, M. Muccini, V. Biondo, C. Soldano, G. Generali, S. Toffanin, M. Melucci, *J Mater Chem C. Mater* **2016**, *4*, 9411.
[61] Z. Gao, C. S. Lee, I. Bello, S. T. Lee, R. M. Chen, T. Y. Luh, J. Shi, C. W. Tang, *Appl. Phys. Lett.* **1999**, *74*, 865.
[62] S. M. K. A. Naqvi, M. F. Baig, T. Farid, Z. Nazir, S. A. H. Mohsan, Z. Liu, W. Cai, S. Chang, *Nanomaterials* **2023**, *13*, 3020.
[63] L. Ke, S. J. Chua, K. Zhang, N. Yakovlev, *Appl. Phys. Lett.* **2002**, *80*, 2195.
[64] R. Capelli, S. Toffanin, G. Generali, H. Usta, A. Facchetti, M. Muccini, *Nat. Mater.* **2010**, *9*, 496.
[65] G. Generali, F. Dinelli, R. Capelli, S. Toffanin, M. Muccini, *J. Phys. D Appl. Phys.* **2011**, *44*, 224018.
[66] W. A. Koopman, M. Natali, G. P. Donati, M. Muccini, S. Toffanin, *ACS Photonics* **2017**, *4*, 282.
[67] A. Minotto, P. A. Haigh, Ł. G. Łukasiewicz, E. Lunedei, D. T. Gryko, I. Darwazeh, F. Cacialli, *Light Sci. Appl.* **2020**, *9*, 70.
[68] A. Minotto, I. Bulut, A. G. Rapidis, G. Carnicella, M. Patrini, E. Lunedei, H. L. Anderson, F. Cacialli, *Light Sci. Appl.* **2021**, *10*, 18.
[69] J. Kang, J. B. Son, G. W. Kim, S. Bae, K. S. Min, S. Sul, W. S. Jeon, J. Jang, G. S. Park, J. K. Shin, J. H. Kwon, S. K. Kim, *Physica Status Solidi (A) Applications and Materials Science* **2020**, *217*, 2000081.
[70] Z. Gan, R. Liu, R. Shinar, J. Shinar, *Appl. Phys. Lett.* **2010**, *97*, 113301.
[71] P. Debye, J. O. Edwards, *J. Chem. Phys.* **1952**, *20*, 236.
[72] G. Paasch, T. Lindner, C. Rost-Bietsch, S. Karg, W. Riess, S. Scheinert, *J. Appl. Phys.* **2005**, *98*, 084505.
[73] J. Zaumseil, R. H. Friend, H. Sirringhaus, *Nat. Mater.* **2006**, *5*, 69.
[74] J. Zaumseil, H. Sirringhaus, *Chem Rev.* **2007**, *107*, 1296.
[75] S. Y. Cho, S. Y. Kim, S. Jeon, R. Choi, J. H. Lee, *Appl. Phys. Lett.* **2019**, *115*, 043301.
[76] Q. Gong, W. Zhang, J. He, F. Ma, L. Song, L. Cheng, J. Zhang, L. Wang, Y. Hu, *Opt. Express* **2023**, *31*, 2480.
[77] M. C. Gwinner, D. Kabra, M. Roberts, T. J. K. Brenner, B. H. Wallikewitz, C. R. McNeill, R. H. Friend, H. Sirringhaus, *Adv. Mater.* **2012**, *24*, 2728.
[78] P. Pracht, F. Bohle, S. Grimme, *Phys. Chem. Chem. Phys.* **2020**, *22*, 7169.
[79] C. Bannwarth, S. Ehlert, S. Grimme, *J. Chem Theory Comput.* **2019**, *15*, 1652.
[80] S. Grimme, *J. Chem Theory Comput.* **2019**, *15*, 2847.
[81] F. Neese, *Wiley Interdiscip. Rev. Comput. Mol. Sci.* **2012**, *2*, 73.
[82] F. Neese, *Wiley Interdiscip. Rev. Comput. Mol. Sci.* **2018**, *8*, e1327.
[83] A. Schäfer, H. Horn, R. Ahlrichs, *J. Chem Phys.* **1992**, *97*, 2571.
[84] F. Weigend, R. Ahlrichs, *Phys. Chem. Chem. Phys.* **2005**, *7*, 3297.
[85] A. D. Becke, *J. Chem. Phys.* **1992**, *96*, 2155.
[86] S. Grimme, J. Antony, S. Ehrlich, H. Krieg, *J. Chem. Phys.* **2010**, *132*, 154104.
[87] B. De Souza, F. Neese, R. Izsák, *J. Chem. Phys.* **2018**, *148*, 034104.
[88] Y. Zhao, D. G. Truhlar, *Theor. Chem Acc.* **2008**, *120*, 215.
[89] V. Barone, M. Cossi, *Quantum Calculation of Molecular Energies and Energy Gradients in Solution by a Conductor Solvent Model*, **1998**.